



(UV, VIS) Laboratory evaluation of the lidar depolarization ratio of freshly emitted soot aggregates from pool fire in ambient air at exact backscattering angle

Lucas Paulien, Romain Ceolato, Frédéric Fossard, Patrick Rairoux, Alain Miffre

► To cite this version:

Lucas Paulien, Romain Ceolato, Frédéric Fossard, Patrick Rairoux, Alain Miffre. (UV, VIS) Laboratory evaluation of the lidar depolarization ratio of freshly emitted soot aggregates from pool fire in ambient air at exact backscattering angle. *Journal of Quantitative Spectroscopy and Radiative Transfer*, 2021, 260, pp.107451. <10.1016/j.jqsrt.2020.107451>. <hal-03143761>

HAL Id: hal-03143761

<https://hal.science/hal-03143761v1>

Submitted on 15 Dec 2022

HAL is a multi-disciplinary open access archive for the deposit and dissemination of scientific research documents, whether they are published or not. The documents may come from teaching and research institutions in France or abroad, or from public or private research centers.

L'archive ouverte pluridisciplinaire **HAL**, est destinée au dépôt et à la diffusion de documents scientifiques de niveau recherche, publiés ou non, émanant des établissements d'enseignement et de recherche français ou étrangers, des laboratoires publics ou privés.



Distributed under a Creative Commons CC BY-NC 4.0 - Attribution - Non-commercial use - International License

(UV, VIS) laboratory evaluation of the **lidar** depolarization ratio of freshly emitted soot aggregates from pool fire in ambient air at exact backscattering angle

Lucas Paulien^{1,2}, Romain Ceolato¹, Frédéric Fossard³, Patrick Rairoux⁴ and Alain Miffre⁴

¹ONERA, The French Aerospace Lab, Université de Toulouse, FR 31055, France

²Laboratoire EM2C, CentraleSupélec, Université Paris-Saclay, Gif-sur-Yvette, 91192, France

³Université Paris-Saclay, ONERA, CNRS, Laboratoire d'Etude des Microstructures, 92322 Chatillon, France

⁴University of Lyon, Université Claude Bernard Lyon 1, CNRS, Institut Lumière Matière, F-69622, Villeurbanne, France

Corresponding author: A. Miffre (alain.miffre@univ-lyon1.fr)

Abstract

In this paper, a controlled-laboratory experiment is carried out to evaluate the **lidar** depolarization ratio of freshly emitted soot aggregates in the exact backward scattering direction at 180.0°. The experiment is performed at two wavelengths simultaneously, namely 355 and 532 nm, often used in polarimetric lidar remote sensing. The soot aggregates are generated from a kerosene JET A-1 pool fire in laboratory ambient air and microscopic images confirm the fractal morphology of generated soot aggregates. Then, the Superposition T-Matrix (STM) method is applied to numerically simulate the soot aggregates backscattering properties for different soot particles refractive indices, monomer radii and monomer numbers. The range of these parameters **which ensures** the lowest discrepancy between the laboratory measurement and the STM-computations is discussed within experimental and numerical error bars. *We find that the polydisperse monomers model gives an overall better evaluation of the ratio $F_{22}(\pi)/F_{11}(\pi)$. In the polydisperse case, our numerical and laboratory experimental findings agree at both wavelengths for a refractive index $m = 2.65 + i1.32$ and monomer number $N_m > 40$ at a mean monomer radius of $r_p = 30$ nm ($N_m > 160$ at $r_p = 27.5$ nm).* We believe this work may be useful for the light scattering and remote sensing communities and may also help future studies aimed at better understanding the impact of soot particle aggregates on the Earth's climate, which still needs to be precisely quantified.

Keywords

Backscattering; laboratory; soot particles; **lidar depolarization ratio**; polarimetry; STM.

1. Introduction

Soot aggregates are particles emitted during the incomplete combustion of organic matter (e.g. biomass, hydrocarbon fuel), through natural and anthropogenic processes. These particles are formed by clustered **nearly**-spherical primary particles which form irregularly-shaped aggregates. Different combustion processes can lead to variations in the aggregates size and structure [1], the latter being usually described with a fractal model [2], [3]. Moreover, when airborne, the soot particles can induce air-quality issues and **are part of complex** atmospheric chemistry **processes** [4]–[6]. Indeed, the molecular composition and sub-micronic size of soot aerosols can induce pulmonary and arterial diseases, as well as cancers [4], [7]. Soot particles also contribute to the Earth's climate warming by inducing a positive radiative forcing, through both direct and indirect effects. However, the uncertainty on these effects remains high [8], [9] as these impacts are partly dependent on the morphology of the particles [10]. Hence, the detection of soot particles and their in-situ characterization are required to better understand and predict their impact on air-quality and on the Earth's climate, by reducing the corresponding uncertainties.

In this context, the scattering of light in the backward direction (*i.e.* backscattering) is of utmost importance for remote sensing applications such as Light Detection and Ranging (lidar). The inversion of the received lidar signal and the analysis of the resulting lidar products (*i.e.* backscattering and extinction coefficients) allows retrieving the particles concentration, the particles size distribution or morphological properties [11], [12]. The lidar problem is however under-determined as several microphysical parameters (*e.g.* size distribution, radius) can lead to the same backscattered radiation [13], [14]. Hence, lidar inversion algorithms and analysis require a-priori knowledge of several input parameters, such as the lidar ratio or the Lidar Depolarization Ratio (LDR), as emphasized in [15, 19]. The LDR is defined as the ratio between the cross and co-polarized components of the backscattered radiation. It can be used to specify the type of particle present in the medium [16], [17]. To detect soot particles with a lidar is however a challenging task, mainly due to the complex morphology of soot particle aggregates. Recently, Miffre et al. [18] remotely measured the very low Planck thermal radiation emitted by absorbing soot particles by incandescence, after their heating by the lidar laser source. Though promising, as being a clear signature of the absorption process, this methodology is rather difficult to apply during daytime. Hence, complementary methodologies have been developed such as polarization lidars, by considering the low depolarization of soot particles [19]. However, deriving the soot particles depolarization ratio from atmospheric lidar measurements is difficult, at least because the measured depolarization is nevertheless that of a particles mixture: as explained in [12], [15], [17], the measured depolarization ratio may indeed differ from that specific to the soot particles under study.

To address the scattering properties of soot particle aggregates is also complex from a numerical point of view, mainly due to their complex shape. Numerical models are extensively described in the literature and interested readers can refer to recent papers by Kahnert and Kanngießer [20], Liu and Mishchenko [21], [22]. These numerical models can be used to study the effect of different morphologies on the radiative properties in the lidar backward scattering direction. Indeed, the Lorenz-Mie theory can be applied to calculate the radiative properties of the equivalent sphere based on the particles morphological properties but has shown poor accuracy when applied to soot aggregates [23], [24]. The Rayleigh-Debye-Gans for Fractal Aggregates (RDGFA) theory is also commonly used to compute soot aggregates scattering properties [25]. This method has shown accuracy in the computation of angle-integrated radiative properties (*e.g.* extinction cross section) but its applicability is limited when considering large size parameters and angle-dependent features such as the scattering matrix elements [26]. The Lorenz-Mie theory and the RDGFA method also do not reproduce the particles LDR in the lidar backward scattering direction. The Discrete Dipole Approximation method allows the computation of the electromagnetic field scattered by particles of arbitrary shape [10], [27], [28]. Although this method is often used as a reference to assess the accuracy of other numerical methods, its highly demanding computational cost makes it rather difficult to implement in numerical studies covering a large range of morphological parameters and number of aggregate realizations. Finally, the Superposition T-Matrix (STM) method can also be used to compute soot aggregates scattering properties [29], providing that the particles structures are composed exclusively of non-overlapping spheres. Despite these major recent advances, the underlying assumptions, inherent to numerical simulations, should be discussed.

In this context, and to face the problem of backscattering by irregularly-shaped particles, controlled-laboratory experiments are proposed to evaluate the lidar particles depolarization ratio [30], [31]. Strictly speaking however, all these experimental set-ups do not operate in the lidar backward scattering direction corresponding to the π -angle, which may lead to potentially quite considerable errors in the evaluation of the LDR [32]. Indeed, at scattering angles approaching the π -angle, the LDR is indeed determined from the ratios F_{22}/F_{11} and F_{21}/F_{11} of the scattering matrix elements, which a priori depend on the scattering angle in a way that still needs to be quantified. In particular, it is only at strict π - backscattering angle that F_{12} is

null. Hence and as discussed in [32], [33], precise evaluations of the lidar LDR of soot particles can only be performed at exact backscattering angle, by precisely evaluating the ratio F_{22}/F_{11} at specific backscattering angle of 180.0° . If precise enough, such laboratory-measurements can then be used to discuss, within experimental error bars, on the ability of existing light-scattering numerical models to faithfully reproduce the LDR of soot particles.

In recent papers [22], [34], lidar measurements of the LDR of stratospheric smoke have been compared with numerical results using spheroid morphological models with varying size, aspect ratio and refractive indices. In [35], the scattering matrix elements of soot particles have been measured from 5° to 175° at 532 nm wavelength, and subsequently modelled using the STM method with different set of morphological parameters and complex refractive index. A different approach is used in this study, where the LDR of freshly emitted soot aggregates is for the first time to our knowledge evaluated in a controlled-laboratory experiment operating at the exact backscattering angle of 180.0° . Moreover, the experiment is achieved at two wavelengths simultaneously, namely $\lambda_{UV} = 355$ nm and $\lambda_{VIS} = 532$ nm, often used in polarimetric lidar remote sensing [16], [17], [19], [36]. The soot particles are emitted from the combustion of a kerosene JET A-1 pool fire in laboratory ambient air. Because of the vicinity of the emission source, we refer to these particles as freshly emitted soot aggregates. Transmission Electron Microscopy (TEM) images of the freshly emitted soot aggregates are also provided and from these TEM-observations, we find the fractal-like morphological model to be the most relevant in our case, as it closely describes our observed structures. Then, using the STM method, several ensembles of freshly emitted soot aggregates scattering properties are computed with varying morphological parameters and refractive indices, before identifying the soot parameters (refractive indices, radii and number of monomers) ensuring the lowest discrepancy between the laboratory-measured and the numerically-computed LDR-values. The paper is hence organized as follows. Section 2 is dedicated to our laboratory experimental set-up at the exact backscattering angle of 180.0° , based on the scattering matrix formalism. Section 3 presents our LDR-laboratory measurements of freshly emitted soot aggregates at wavelengths λ_{UV} and λ_{VIS} . The numerical methods are then presented in Section 4, where the LDR is numerically computed at both wavelengths by applying the STM method. Finally, the soot parameters (refractive indices, radii and number of monomers) ensuring the lowest discrepancy between the laboratory-measured and the numerically-computed LDR-values are discussed in Section 5, followed by our conclusions and outlooks.

2. Light backscattering by soot particles from pool fire

2.1 Scattering matrix formalism

Considering an incident electromagnetic wave defined by the Stokes vector I^{inc} , with a direction vector defined as \mathbf{n}^{inc} on an arbitrary particle ensemble, the scattered wave, with propagation direction defined by the vector \mathbf{n}^{sca} , is defined as :

$$I^{sca}(r\mathbf{n}^{sca}) = \frac{1}{r^2} \mathbf{Z}(\mathbf{n}^{sca}, \mathbf{n}^{inc}) I^{inc} \quad (1)$$

where r is the distance from the scattering event to the observer and \mathbf{Z} is the 4×4 scattering phase matrix specific to the particles orientation, shape and refractive index. The orientation averaging [37] of the normalized phase matrix allows to reduce the two propagation vectors dependence to only one scalar property as [38]:

$$\langle \mathbf{Z}(\mathbf{n}^{sca}, \mathbf{n}^{inc}) \rangle_{\zeta} = \mathbf{f}(\theta) = \begin{pmatrix} F_{11}(\theta) & F_{12}(\theta) & 0 & 0 \\ F_{21}(\theta) & F_{22}(\theta) & 0 & 0 \\ 0 & 0 & F_{33}(\theta) & F_{34}(\theta) \\ 0 & 0 & F_{43}(\theta) & F_{44}(\theta) \end{pmatrix} \quad (2)$$

where θ is the scattering angle and the notation $\langle \rangle_{\zeta}$ refers to orientation averaging. In the strict backward scattering direction (i.e. $\theta = \pi$), the phase matrix further simplifies to [39] and exhibits only two non-vanishing elements, namely $F_{11}(\pi)$ and $F_{22}(\pi)$. The lidar depolarization ratio (LDR) of soot particles from pool fire is then determined by the ratio $F_{22}(\pi)/F_{11}(\pi)$ of the scattering matrix elements:

$$\text{LDR} = \delta(\pi) = \frac{1 - F_{22}(\pi)/F_{11}(\pi)}{1 + F_{22}(\pi)/F_{11}(\pi)} \quad (3)$$

In this study, the ratio $F_{22}(\pi)/F_{11}(\pi)$ has been experimentally evaluated in laboratory at two wavelengths. Numerical computations of this ratio are also conducted in order to assess the agreement between simplified numerical models and laboratory experimental findings. From Eq. (3), it is clear that increasing the ratio $F_{22}(\pi)/F_{11}(\pi)$ leads to a decrease in the corresponding LDR.

2.2 Laboratory experiment for evaluating the soot particles depolarization

As schemed in Fig 1, light backscattering by soot particles from pool fire is simultaneously measured at two wavelengths ($\lambda_{UV} = 355$ nm, $\lambda_{VIS} = 532$ nm) by two laboratory polarimeters, each measuring the intensity of the backscattered wave at a given wavelength. The backscattering angle is addressed with accuracy and $\theta = (180.0 \pm 0.2)^\circ$. The principle of this (UV, VIS) controlled-laboratory experiment at exact backscattering angle ($180.0 \pm 0.2^\circ$) has been extensively described in [33] where the same experiment has been used for mineral dust particles embedded in ambient air. As a detailed description is available in this former publication, we here only briefly recall the methodology in order to ease the reading. Following Fig 1, the scattered Stokes vector can be related to the incident Stokes vector by considering the successive Muller matrices corresponding to each optical component present between the light source and the light detector:

$$\mathbf{I}^{sca} = [\mathbf{PBC}][\mathbf{QWP}][\mathbf{F}(\pi)][\mathbf{QWP}][\mathbf{PBC}]\mathbf{I}^{inc} \quad (4)$$

Where $[\mathbf{F}(\pi)]$ is given by Eq. (2) for $\theta = \pi$ and $[\mathbf{QWP}]$ and $[\mathbf{PBC}]$ are the Mueller matrices of the quarter-wave plate and the reflecting polarizing cube respectively. The detected light intensity measured by each polarimeter corresponds to the first component of the scattered Stokes vector. Developing the expression of the different Muller matrices that appear in Eq. (4) for incident light polarized parallel to the scattering plane (e.g. $\mathbf{I}^{inc} = [1, 1, 0, 0]^T$), the intensity of the detected backscattered wave is given by [33]:

$$I(\psi) = I_0 \times [a - b \cos(4\psi)] \quad (5)$$

where the intensity I_0 mainly depends on the intensity of the laser source and on the distance from the detector to the soot particles while the angle ψ is the angle between the fast axis of the quarter-wave plate and the scattering plane. Interestingly, the coefficients a and b are wavelength-dependent as determined by the scattering matrix elements $F_{11}(\pi)$ and $F_{22}(\pi)$: $2a = F_{11}(\pi) + F_{22}(\pi)$ while $2b = 3F_{22}(\pi) - F_{11}(\pi)$. The $I(\psi)$ -curve hence has $a - b = F_{11}(\pi) - F_{22}(\pi)$ for minimum, which is null for spherical particles only. Likewise, the maxima of the $I(\psi)$ -curve are equal to $2F_{22}(\pi)$. Moreover, the a and b coefficients can be precisely evaluated by adjusting the laboratory-measured $I(\psi)$ -values with Eq. (5), as detailed below in

Section 3.2. Precise evaluations of $F_{22}(\pi)/F_{11}(\pi)$ for soot particles embedded in laboratory ambient air can then be retrieved from a and b since:

$$[F_{22}(\pi)/F_{11}(\pi)]_{lab} = (a + b)/(3a - b) \quad (6)$$

As expected, $F_{22}(\pi)/F_{11}(\pi)$ equals unity for spherical particles for which coefficients a and b are equal. Moreover, the LDR of soot particles can then be retrieved from $[F_{22}(\pi)/F_{11}(\pi)]_{lab}$ by applying Eq. (3).

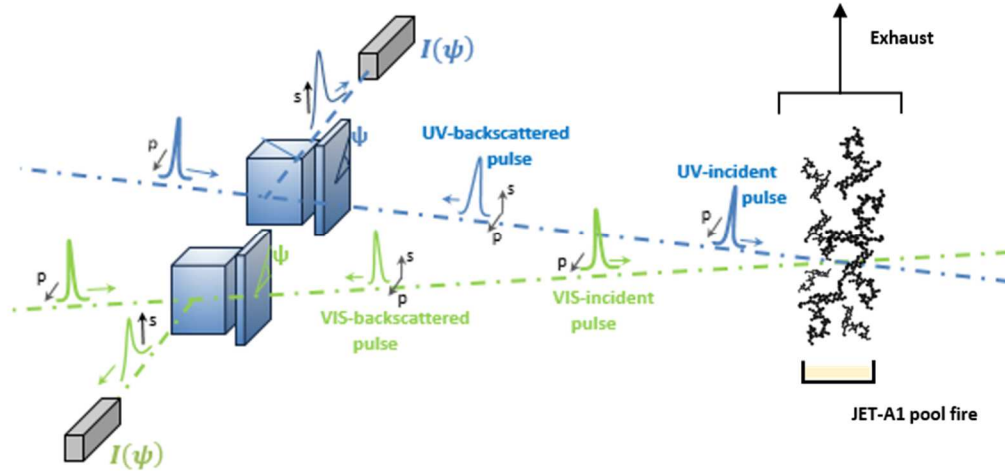


Figure 1 : Principle of the laboratory backscattering experimental set-up to evaluate the particles depolarization ratio LDR in laboratory ambient air, identical to that presented in [33], but here applied to the particles released from a JET A-1 pool fire. In a few words, the experiment relies on two laboratory polarimeters (one at $\lambda_{UV} = 355$ nm in blue, one at $\lambda_{VIS} = 532$ nm in green) operating simultaneously in the exact backward scattering direction $\theta = (180.0 \pm 0.2)^\circ$. Based on the Mueller matrix formalism, each laboratory polarimeter allows precise evaluations of the soot particles LDR by adjusting the variations of the detected scattered intensity $I(\psi)$ with Eq. (5) to retrieve $[F_{22}(\pi)/F_{11}(\pi)]_{lab}$ then the corresponding LDR $\delta_{lab}(\pi)$, by applying Eqs. (3,6), as detailed in Section 3.2 below. A distance of 5 meters separates the pool fire from the detectors.

3. Laboratory light backscattering by freshly emitted soot particles from pool fire

3.1 Soot emitted from small-scale kerosene pool fire

Pool fires are defined as self-sustaining turbulent diffusion flames generated over a plain liquid fuel surface. Such fires are of particular interest for phenomenological investigations of combustion [40], [41]. For the purpose of this study, we have designed a small-scale kerosene pool fire which consists in a round container of kerosene with a diameter of 50 mm and 20 mm height. Such an experimental set-up enables the production of a constant soot emission from a defined volume of fuel. Following theoretical knowledge about liquid pool fire, the pool fire heat release rate and burning duration are evaluated for a kerosene burning rate $m'' = 0.039 \text{ kg} \cdot \text{m}^{-2} \cdot \text{s}^{-1}$. In this study, JET A-1 (NATO code F-35) kerosene was used. Thus, the heat release rate is estimated at 5 kW for a burning duration of 30 seconds. The flame height is comprised between 35 cm and 55 cm estimated from the Heskestad and Thomas method [42], [43]. The light backscattering measurements were carried out for a few seconds after ignition and during the steady burning time of the pool fire combustion.

Soot particles emitted from the small-scale kerosene pool fire have been analyzed by Transmission Electron Microscopy (TEM), as shown in Fig. 2(a). More precisely, particles have been captured and transferred on TEM grids covered by a holey carbon film in order to observe suspended aggregates. TEM grids were placed at the laser height (i.e. 30 cm above

the recipient base), and approximately 3 cm off the axis formed by the container center and the laser beam. The Zeiss LIBRA 200 microscope is equipped with an in-column filter to achieve filtered images and operates at 200 kV. No degradation of the soot structure has been observed during the light backscattering experiment. Typical aggregates, as illustrated in Fig. 2(a), are composed of several tens of monomers with narrow size dispersion. These monomers exhibit a degree of non-sphericity and overlapping. High resolution images have shown that the monomers exhibit an onion-like structure fully graphitized. Due to restraints imposed by the process of particles sampling, the monomer radius reported here represents radii averaged over several TEM grids at different sampling location in the pool fire. Analysis of the TEM image allows the retrieval of the monomer radius size distribution, as displayed in Fig. 2(b). To characterize this size distribution, we use the lognormal size distribution defined as:

$$f(r_p) = \frac{1}{r_p \ln(\sigma_p) \sqrt{2\pi}} e^{-\frac{1}{2} \left(\frac{\ln(r_p) - \ln(R_p)}{\ln(\sigma_p)} \right)^2} \quad (7)$$

where $f(r_p)dr_p$ is the size distribution giving the number of monomers with radius between r_p and $r_p + dr_p$, R_p is the mean radius and σ_p is the monomer radius deviation. This distribution is often used in order to characterize soot aggregates monomers polydispersion [44]. Using this method, we find that the monomer radius size distribution is characterized by a mean radius of $R_p = 27 \text{ nm}$ and a standard deviation of $\sigma_p = 1.1$. This value for primary soot particle size is relatively large compared with soot produced by laminar diffusion flames but remains consistent with previous results obtained from soot emitted by pool fires [45].

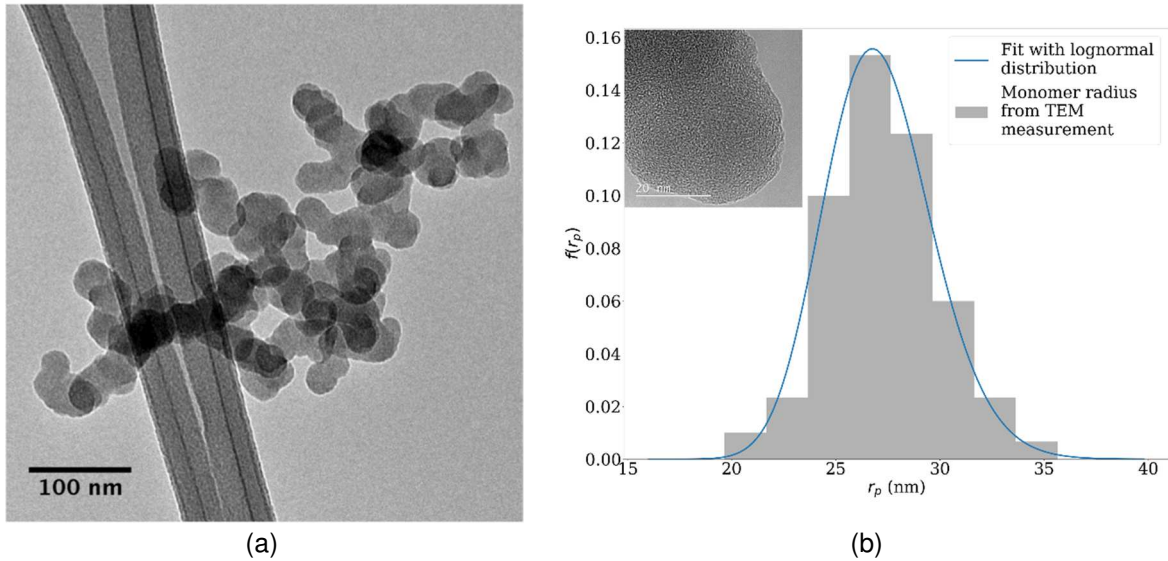


Figure 2: (a) HR TEM image of a soot aggregate generated from our JET A-1 pool fire, (b) Corresponding monomer radius size distribution. In order to represent this distribution, 151 monomers have been characterized. The top-left insert is a zoomed in view of a monomer, showing the onion-like structure.

3.2 Light backscattering by freshly emitted soot particles from pool fire

By applying the experimental set-up presented in Fig. 1, we display in Fig. 3 the variations of the detected backscattered intensity $I(\psi)$ as a function of the modulation angle ψ at wavelength λ_{UV} and λ_{VIS} . Light backscattering from the soot particles generated from the pool fire is distinguished from that due to particles in laboratory ambient air by using pulsed laser light. Special care has been taken to minimize the potential polarization and wavelength cross-talks affecting the detected backscattered light intensity (see [33] for more details). At each wavelength, within our experimental error bars, the detected backscattered intensity

exhibits constant minima, which mean that the shape distribution of the generated soot particles did not vary during the acquisition. Indeed, these minima, which are equal to $F_{11}(\pi) - F_{22}(\pi)$ (see Section 2.2), are a clear optical signature of the soot particles non-sphericity and interestingly, the precision of our experimental set-up allows to unambiguously measure these minima at two wavelengths to evaluate the soot particles LDR at two wavelengths. A precise evaluation of the soot LDR can then be achieved from Fig. 3 where the detected scattered light intensity is recorded for each position of the QWP, to gain in accuracy. Our experimental data points are then adjusted with Eq. (5) to get precise evaluations of the ratio $F_{22}(\pi)/F_{11}(\pi)$ from Eq. (6), as given in Table 1. As a result, the LDR of soot particles released from the pool fire in laboratory ambient air is retrieved from Eq. (3) and is equal to $(11.7 \pm 2.3) \%$ at wavelength λ_{UV} and to $(8.7 \pm 2.1) \%$ at wavelength λ_{VIS} . Table 1 summarizes our findings from this laboratory backscattering experiment.

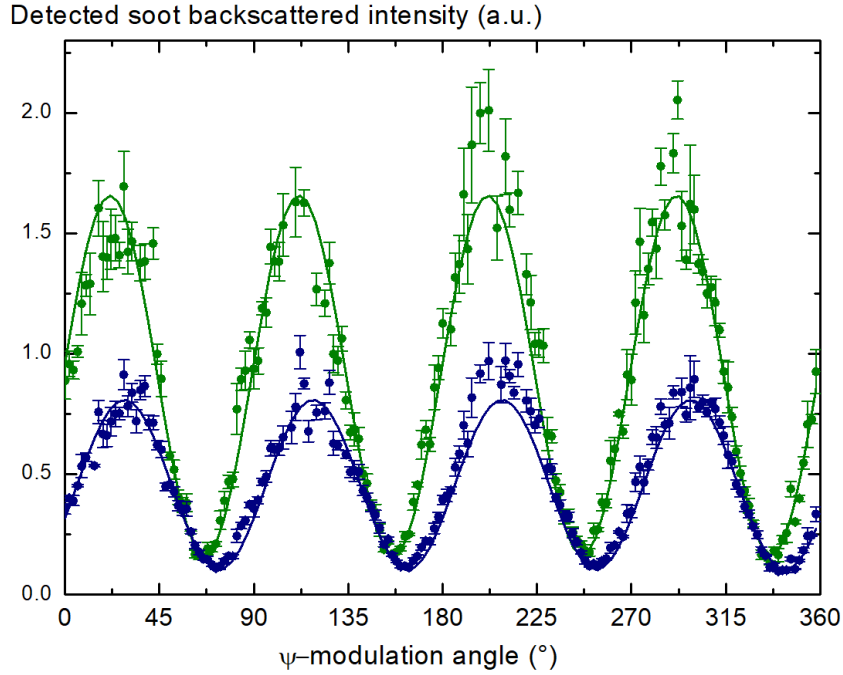


Figure 3 : Detected backscattered light intensity $I(\psi)$ from soot particles (JET A-1) generated in a pool fire at exact backscattering angle of π and wavelengths $\lambda_{UV} = 355$ nm (in blue) and $\lambda_{VIS} = 532$ nm (in green). The experimental data points are adjusted with Eq. (5), *represented in full lines*, to retrieve $(F_{22}/F_{11})_{lab}$ then $\delta_{lab}(\pi)$ by applying Eqs. (3,6).

Table 1 : Evaluation of the ratio $[F_{22}(\pi)/F_{11}(\pi)]_{lab}$ and LDR $\delta_{lab}(\pi)$ of soot particles emitted from at JET A-1 pool fire. *These ratios are specific to the freshly emitted soot aggregates from JET-A1 pool fire. LDR measurement derived from airborne or spaceborne lidar instruments may differ as explained in [12], [15], [17].*

Wavelength (nm)	$[F_{22}(\pi)/F_{11}(\pi)]_{lab}$	LDR $\delta_{lab}(\pi)$ (%)
355	0.79 ± 0.03	11.7 ± 2.3
532	0.84 ± 0.03	8.7 ± 2.1

4. Numerical backscattering simulations

4.1 Soot fractal aggregate models and scattering matrix computation

In order to model the soot morphology, two shape models have been considered. As a first shape model, the aggregates morphology is described by monodisperse spheres in point contact. The morphology of soot aggregates is described using a fractal model [2], [3], and this monodisperse model is described using the following equation:

$$N_m = k_f \left(\frac{R_g}{r_m} \right)^{D_f} \quad (8)$$

where N_m is the number of monomers (i.e. spherical primary particles), k_f is the fractal prefactor, R_g is the radius of gyration, r_m is the monomer radius and D_f is the fractal dimension.

For aggregates formed by polydisperse monomers, a similar expression is used as [46] :

$$N_m = k_f \left(\frac{R_g}{r_p} \right)^{D_f} \quad (9)$$

where r_p is the monomers geometric mean radius.

Monodisperse aggregates have been generated using a tunable cluster-cluster aggregation algorithm [47], [48], allowing to predetermine the morphological parameters as defined in Eq. (8). In order to be consistent with aggregates generated through classical Diffusion-Limited Cluster Aggregation (DLCA) algorithms, we generated aggregates with a fractal dimension of $D_f = 1.8$ and a fractal prefactor of $k_f = 1.3$ [49], with varying numbers of monomers and monomer radii. Using this algorithm, the generated aggregates present a monodisperse radius size distribution. In this method, the monomer radius has been varied from $r_m = 10$ nm to $r_m = 30$ nm with steps of $\Delta R_m = 2.5$ nm. The monomer numbers have been varied from $N_m = 20$ to $N_m = 200$ with steps of $\Delta N_m = 20$. For each set of morphological parameters, 50 aggregates have been generated.

The second shape model is also described using a fractal model. However, the size distribution of the primary particles is accounted for, based on our TEM-laboratory observations. This second method replicates the monomer size distribution observed using the TEM measurements, in which case the aggregates have been generated using the FracVAL code [50]. This numerical program allows generating aggregates with a fixed set of morphological parameters (e.g. number of monomers, fractal dimension) and with either a monodisperse or a polydisperse monomer size distribution. The monomer radius size distribution is described by the lognormal function as defined in Eq. (7). Each aggregate has been generated with a fractal dimension of $D_f = 1.8$ and fractal prefactor $k_f = 1.3$ and a standard deviation of $\sigma = 1.1$. Moreover, the number of monomers has been varied within $N_m \in [20, 200]$ with a step of $\Delta N_m = 20$, and the mean monomer radius within $r_p \in [10, 30]$ with steps of $\Delta r_p = 2.5$ nm. 50 aggregates are generated for each set of morphological parameters and are then gathered into ensembles.

To summarize, Figure 4 presents two examples of aggregates generated with a monodisperse (Figure 4(a)) and a polydisperse (Figure 4(b)) monomer radius size distribution, both with a number of monomers of $N_m = 100$. In Figure 4(b) is also represented the monomer radius size distribution of the aggregates generated with the FracVAL code, using the previously defined parameters.

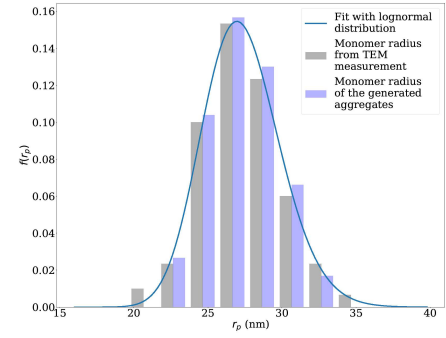


Figure 4 : Examples of generated aggregate with a monodisperse size distribution (a) and a polydisperse size distribution (b). For the polydisperse case, the TEM-observed size distribution (in grey) is compared with that from numerically-generated aggregates (in blue).

The Superposition T-Matrix (STM) method is here used for the computation of soot fractal aggregate scattering properties [29], [51], [52]. This method consists in expressing the scattered field by an assembly of spheres as the superposition of the scattered field by each sphere. Both incoming and outgoing field of each sphere is expressed using Vector Spherical Wave Function (VSFW). The Transition Matrix (T-Matrix), links the outgoing VSFW expansion coefficient to those of the incoming VSFW, therefore considering the coupling between the different spheres. The Multiple Sphere T-Matrix (MSTM) code [53] has been used in order to compute the scattering matrix of soot fractal aggregates. This code takes as inputs the position of each primary particles composing the aggregates, as well as their refractive index and size parameter.

For both shape models, the orientation-averaged ratio $(F_{22}/F_{11})_{num}$ of each individual aggregate is computed using the MSTM code. Results are then averaged according to the set of morphological parameters used in the generation of the aggregates. Hence, in the numerical study, we report results of ensembles of aggregates with same morphological parameters and the associated numerical standard deviation. In order to compute the scattering matrix of the generated aggregates, the complex refractive index is needed. A wide range of complex refractive indices of soot particles are reported in the literature, and the refractive index of the particles generated under the conditions of the experiment described in Section 3 is unknown. In order to cover the range of possible indices, several values of the soot complex refractive index are used during the computations: $m = 1.16 + i0.71$, $m = 1.61 + i0.74$, $m = 1.68 + i0.93$, $m = 1.81 + i0.76$, $m = 2.15 + i0.8$ and $m = 2.65 + i1.32$. These indices are used for both the UV and the VIS computation. The choice of these values is motivated by an already existing study [54] aiming, among other things, at studying the impact of the optical index on the depolarization ratio. All computations are operated within the random orientation settings. Indeed, as the particles are measured in ambient air and in the close vicinity of the pool-fire, the airflow resulting from the combustion process may prevent the particles from keeping a preferred orientation during the backscattering experiment, especially at this size range.

4.2 Numerical results

Figure 5 presents the results of the numerical modelling of the ratio $(F_{22}/F_{11})_{num}$, together with the corresponding LDR values derived from Eq. (3). These numerical results show several trends across all subfigures. First, we can observe smaller ratios as the monomer radius is increased, which implies that soot fractal aggregates with large monomers produces larger lidar depolarization ratio at both wavelengths. A wavelength dependence of the ratio can also be observed. Indeed, at constant morphological parameters and refractive index, the LDR at

532 nm wavelength is lower than at 355 nm. The chosen complex refractive index also induces large variation of the $(F_{22}/F_{11})_{num}$ ratio and consequently of the LDR. Both real part and imaginary part increase induce larger LDR. Finally, in some cases, a dependence on the number of monomers can be observed. Aggregates with a number of monomers under 80 show a decrease in the ratio $(F_{22}/F_{11})_{num}$ with increasing monomer number. In the other cases, the variation is less significative. These numerical results are consistent with results present in the literature as in [21], [51], [54].

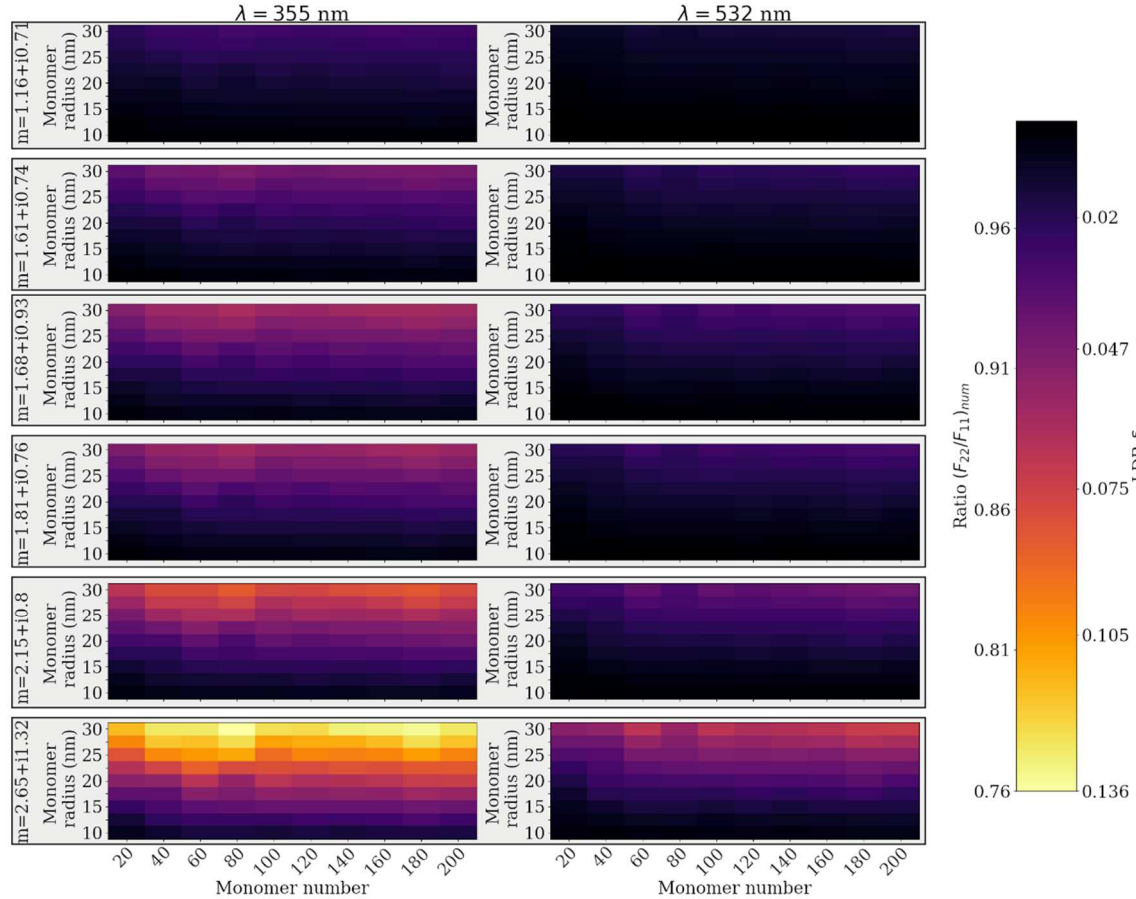


Figure 5 : Numerical results of the ratio $(F_{22}/F_{11})_{num}$ and LDR for ensembles of aggregates formed by monodisperse monomers. The column of subplots refers two different wavelengths, while the rows refer to different refractive index. Inside the figure themselves, the x-axis represents variable monomer number, and the y-axis represents variable monomer radius. The colour scale indicates variation in the numerically computed ratio $(F_{22}/F_{11})_{num}$ and LDR.

The numerical results for the ensembles of aggregates formed by polydisperse monomers are presented in Figure 6. As in the monodisperse case, the F_{22}/F_{11} ratio decreases as the refractive index increases and also as the monomer radius or number increases. Compared with the monodisperse results presented in Figure 5, results for the polydisperse case present slightly lower F_{22}/F_{11} values (i.e. higher LDR). In [54], a slight decrease of the LDR with polydispersity is reported. However, the author used a normal monomer radius size distribution function, in comparison with the lognormal function used in this study, which could explain the discrepancy between our results. This is further supported by the results presented in [55] using a lognormal distribution. Polydisperse results also present an almost monotonic decrease of ratio F_{22}/F_{11} with monomer number, in contrary to the monodisperse results where more variability is present. We attribute this smoothing effect to the polydispersity of the monomer radii.

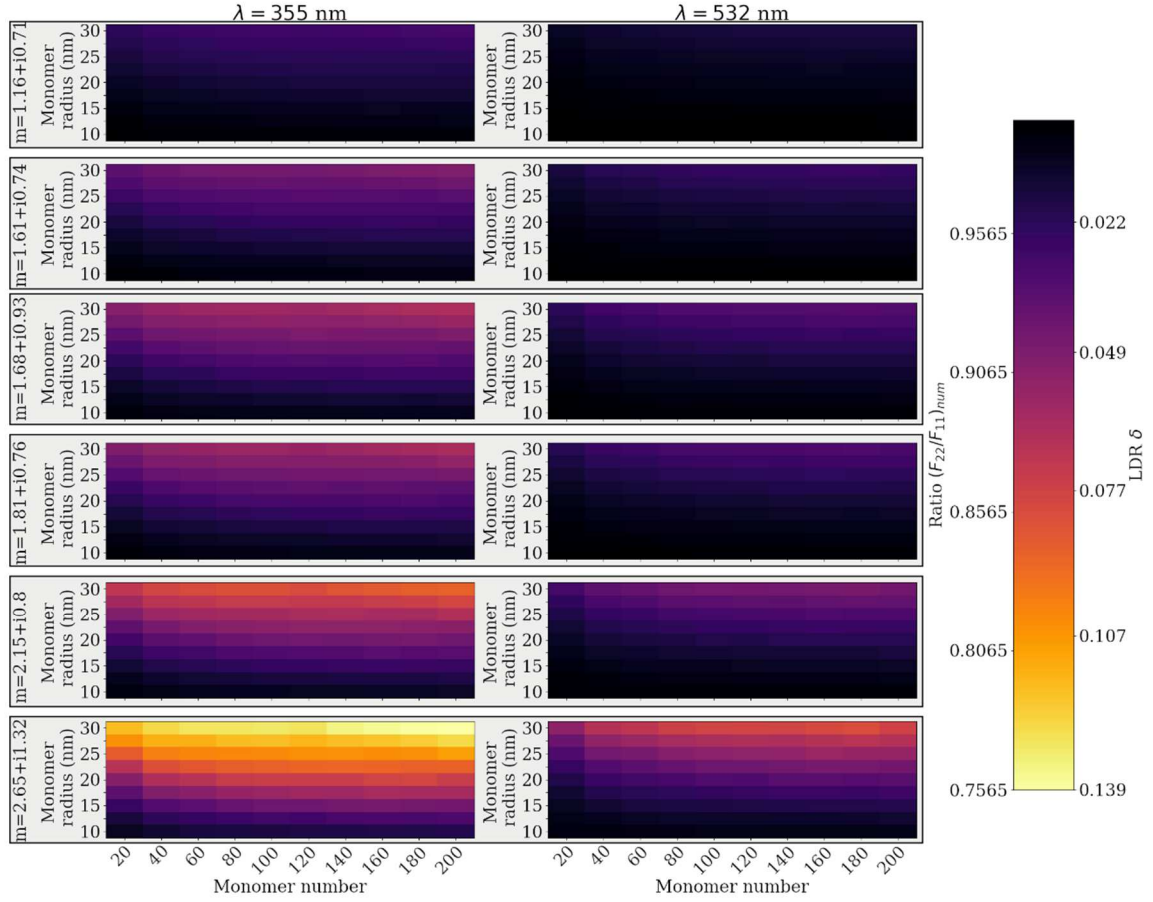


Figure 6 : Numerical evaluation of the ratio $(F_{22}/F_{11})_{num}$ and LDR for *ensembles of aggregates formed by polydisperse monomers*. The column of subplots refers two different wavelengths, while the rows refer to different refractive index. Inside the figure themselves, the x-axis represents variable monomer number, and the y-axis represents variable monomer radius. The colour scale indicates variation in the numerically computed ratio $(F_{22}/F_{11})_{num}$ and LDR.

5. Discussion

In order to assess the discrepancies between the laboratory-measured $(F_{22}/F_{11})_{lab}$ and the numerically-computed $(F_{22}/F_{11})_{num}$ ratios, we introduce the percent disagreement, defined as :

$$\kappa = 100 * \frac{|(F_{22}/F_{11})_{num} - (F_{22}/F_{11})_{lab}|}{(F_{22}/F_{11})_{lab}} \quad (10)$$

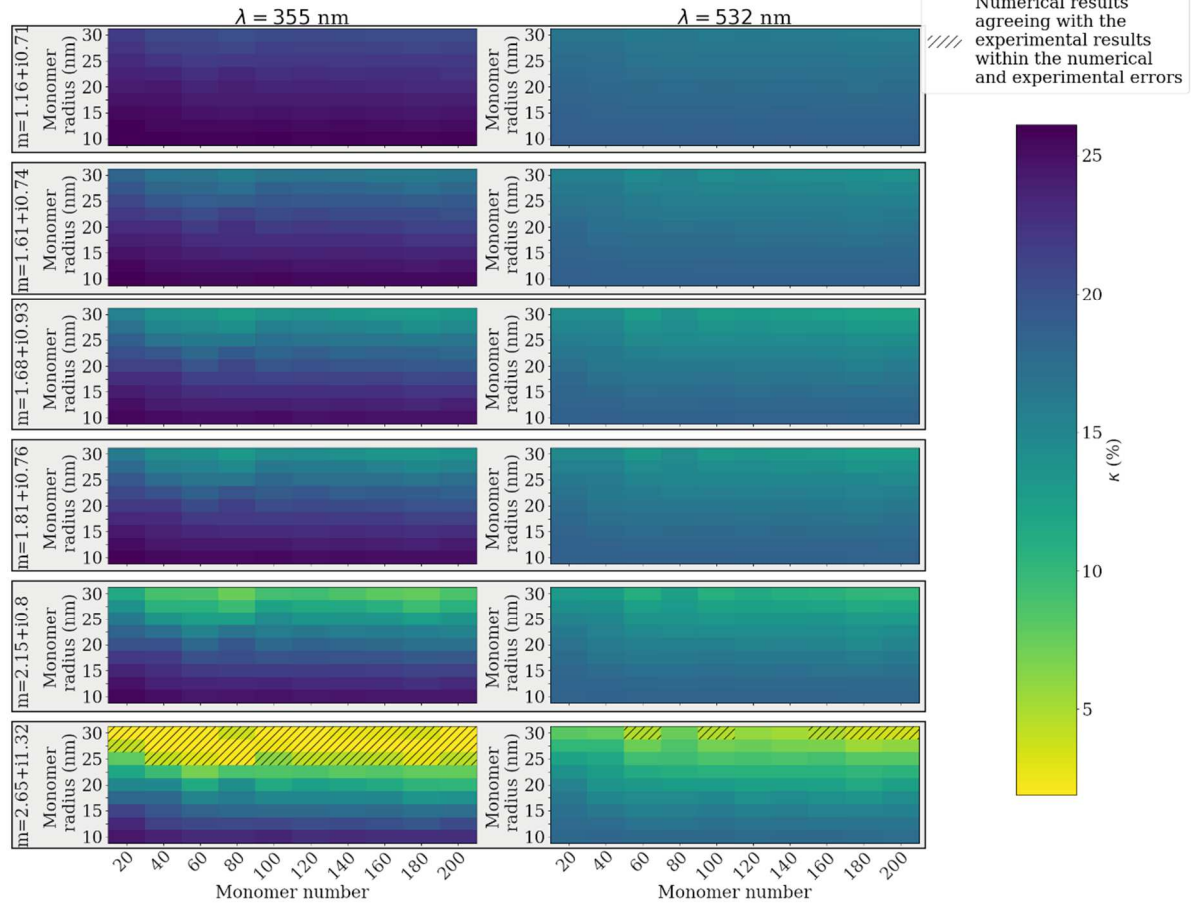


Figure 7 : Discrepancy κ between the laboratory and numerical experiments for monodisperse aggregates (colour scale, with better agreement as the value closes to 0, in yellow). The column of subplots refers two different wavelengths, while the rows refer to different refractive index. Inside the figure themselves, the x-axis represents variable monomer number, and the y-axis represents variable monomer radius.

In Fig. 7 is represented the percent disagreement κ between the numerical and experimental results when monodisperse aggregates are considered. The dashed area represents the range of numerical input parameters (*i.e.* complex refractive index, monomer radius, monomer number) which reproduce the experimental results within the numerical and experimental errors. At 355 nm wavelength, we can observe one main range of agreement. Using a complex refractive index of $m = 2.65 + i1.32$, the soot aggregates with monomer radius $r_m \geq 25$ nm also show good agreement, with the number of monomers within $N_m \in [20, 200]$. At 532 nm wavelength, the results noticeably differ. Indeed, the range of parameters that reproduces the laboratory experimental results is more reduced; only the computation using a complex refractive index of $m = 2.65 + i1.32$, with monomer radius of $r_m = 30$ nm and monomer number $N_m = 60, 100$ and within $N_m \in [160, 200]$ is able to reproduce the experimental results. As stated in Section 2.2, $(F_{22}/F_{11})_{lab}$ has been experimentally evaluated simultaneously at 355 and 532 nm wavelengths. This indicates that a unique ensemble of soot aggregates is responsible for the observed F_{22}/F_{11} ratio and LDR. We may then expect the agreeing numerical results to have the same morphological parameters at both wavelengths. We can then reduce the range of agreement of the morphological parameters (*i.e.* N_m and r_m) by considering only those which coincide at both 355 nm and 532 nm wavelengths. Hence, the ensemble of monomer radius $r_m = 30$ nm and monomer number $N_m = 60, 100$ and within $N_m \in [160, 200]$ are the only ensembles reproducing the experimental results.

Likewise, the κ -values for the polydisperse aggregates results are presented in Fig. 8. Results are similar to those observed in the monodisperse case at 355 nm wavelength, but present differences at 532 nm wavelength. At 355 nm wavelength, results are in agreement for ensembles of monomer radius $r_p \geq 25$ nm and with monomer number within $N_m \in [20,200]$ with a refractive index of $m = 2.65 + i1.32$. At 532 nm wavelength, the lesser variability in the results induced by the polydispersity causes a clearer range of agreement. For a refractive index of $m = 2.65 + i1.32$, ensembles with monomer radius $r_m = 30$ nm and monomer number $N_m \in [40,200]$ are in agreement, as for ensembles with $r_p = 27.5$ and $N_m \in [160,200]$.

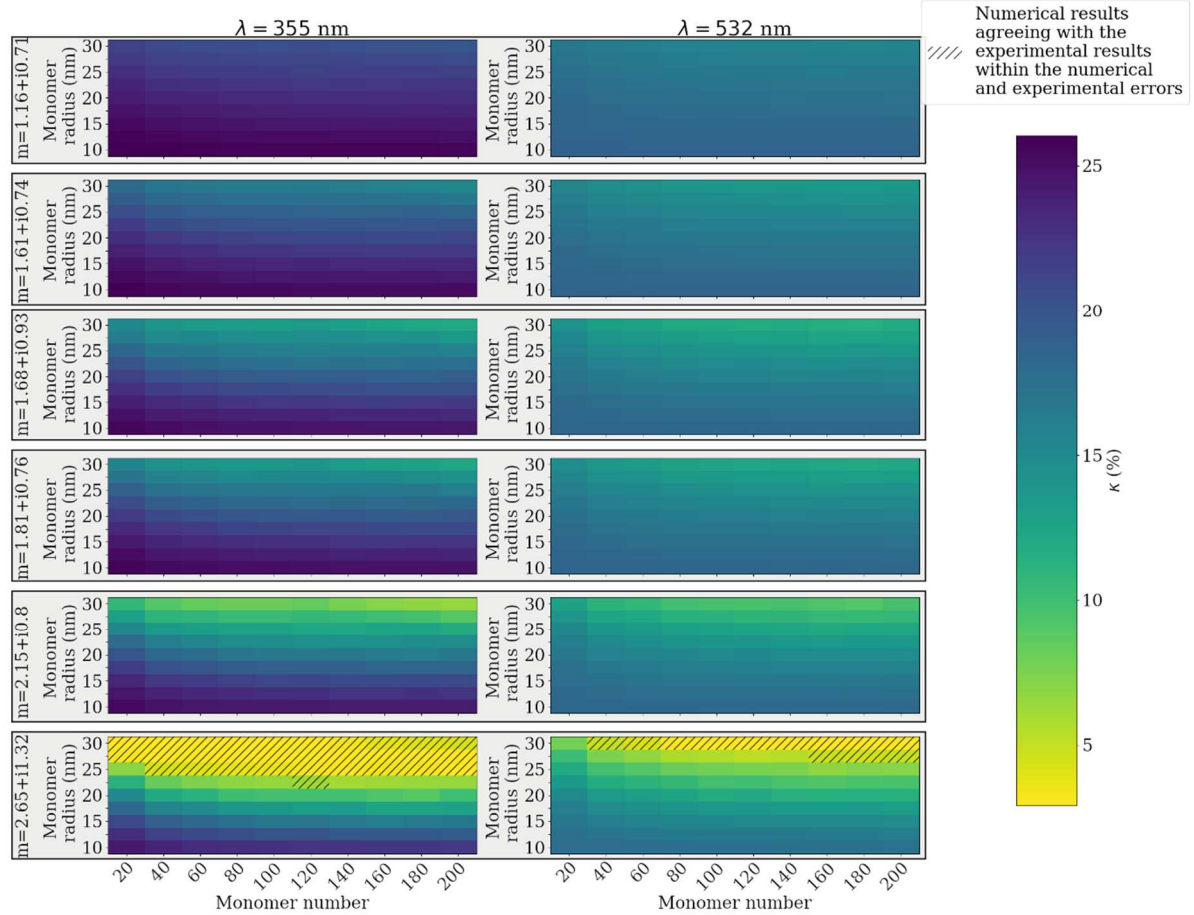


Figure 8 : Discrepancy between the laboratory and numerical experiments for aggregates formed by polydisperse monomers (colour scale, with better agreement as the value closes to 0, in yellow). The column of subplots refers two different wavelengths, while the rows refer to different refractive index. Inside the figure themselves, the x-axis represents variable monomer number, and the y-axis represents variable monomer radius.

During the numerical study, we identified several ensembles which backscattering properties are in agreement with the laboratory results. The monomer radius of these ensembles is consistent with results from the TEM-measurement. The number of monomers is also in a realistic range. Although the numerical results coincide with the experimental results in these cases, the refractive index used remains very large. Indeed, the complex indices correspond to spark-generated soot [56], which microstructure is composed almost exclusively of amorphous carbon [57]. In comparison, the soot aggregates emitted during our experiment clearly exhibits an onion-like structure. Considering that the inclusion of monomer radius polydispersity did not significantly improve the agreement between the numerical and experimental results, this strongly suggests that the morphological models used in this study are in need of further refinement in order to better interpret the laboratory experimental

measurements. Several morphological effects can be considered in order to do so. Particles overlapping and necking effect (*i.e.* supplementary material at the monomers surface), could produce significant changes of the lidar depolarization ratio. As described in [54], particle overlapping has an effect similar to a decrease in monomer number, while necking produces a scaling effect on the LDR in the forward direction. Still, interrogation remains whether these morphological parameters also produce similar results in the backward scattering direction, and in which proportion. To account for these specific morphological effects, the STM method can't be used during the scattering properties computation. Hence, methods with higher computational cost are required, such as DDA methods, which would strongly reduce the considered number of aggregates realization per ensembles and range of parameters. Spheroidal monomers can also be considered in order to better replicate soot morphology. Wu et al. [58] investigated the effects of both prolate and oblate spheroid monomers on the scattering properties of soot aggregates, and showed a decrease in the F_{22}/F_{11} ratio in the backward scattering direction. This morphology type also requires DDA calculation, as the STM method cannot be used for spheroidal monomers currently. Another possible explanation might involve more complex fractal structures such as soot super-aggregates, which have been recently reported in both pool fires [41] and laminar diffusion flames [59], [60] with large depolarization properties [61]. The multiple scattering effect might also be responsible for an increase in the measured LDR. In dense medium composed of spherical droplets, this effect can be responsible for non-zero values of the LDR [62], whereas in the single scattering framework, spherical particles do not depolarize light in the backward scattering direction [39].

6. Conclusion

In this paper, the LDR of freshly emitted soot particles is evaluated at both 355 and 532 nm wavelength in a controlled-laboratory experiment operating in the exact backward scattering angle of 180.0° . This laboratory experimental set-up allows accurate evaluations of the ratio $F_{22}(\pi)/F_{11}(\pi)$, which in turn leads to the evaluation of the corresponding LDR. We report values of $\delta_{UV} = (11.7 \pm 2.3) \%$ at wavelength $\lambda_{UV} = 355$ nm and to $\delta_{VIS} = (8.7 \pm 2.1) \%$ at wavelength $\lambda_{VIS} = 532$ nm, for soot particles generated from a pool fire of JET A-1 in laboratory ambient air. In complement, a numerical study is associated to this laboratory measurement. **Considering the TEM measurements, the structure of the soot aggregates is described by a fractal-like model.** Two morphological models for freshly emitted soot aggregates are used to simulate the soot aggregates structure. Using these morphologies, the scattering properties are computed with the MSTM code. *We find that the morphological model of aggregates formed by polydisperse monomers provides an overall better performance than the monodisperse monomers model. Moreover, in the polydisperse case, the laboratory findings are reproduced at both wavelengths only with the highest considered refractive index ($m = 2.65 + i1.32$) and for monomer number $N_m \geq 40$ with mean monomer radius of $r_p = 30$ nm ($N_m > 160$ at $r_p = 27.5$ nm).* This supports the use of more realistic morphological models when computing soot aggregates backscattering properties and the independent measurement of the complex refractive index of soot particles, at the aggregate and monomer scale. As we do not have direct evidence of the random orientation of the particles, complementary experiments should be performed to tackle this specific issue, which is however beyond the scope of this paper. Likewise, the laboratory experiment may be further improved by analyzing other soot particle aggregates, and by evaluating other radiative properties such as the asymmetry parameter or the single-scattering albedo. This work is however beyond the scope of this contribution. Still as is, the lidar remote sensing community may use our contribution to better interpret polarimetric lidar signals of freshly emitted soot aggregates since, for the first time to our knowledge, accurate laboratory-measured LDR-values of freshly emitted soot aggregates are provided at exact backscattering angle of 180.0° , supported by STM-light backscattering computations.

Acknowledgments

The authors are grateful to D.W. Mackowski and J. Morán for making their respective numerical code available publicly.

D. Cholleton is greatly acknowledged for fruitful discussions.

The authors acknowledge funding from ONERA (PROMETE project), CNRS, SMEMAG doctoral school and GDR SUIE.

References

- [1] L. Tumolva *et al.*, "Morphological and elemental classification of freshly emitted soot particles and atmospheric ultrafine particles using the TEM/EDS," *Aerosol Sci. Technol.*, vol. 44, no. 3, pp. 202–215, 2010, doi: 10.1080/02786820903518907.
- [2] S. R. Forrest and T. A. Witten Jr, "Long-range correlations in smoke-particle aggregates," *J. Phys. A. Math. Gen.*, vol. 12, no. 5, p. L109, 1979.
- [3] Ü. Ö. Köylü, G. M. Faeth, T. L. Farias, and M. G. Carvalho, "Fractal and projected structure properties of soot aggregates," *Combust. Flame*, vol. 100, no. 4, pp. 621–633, 1995, doi: 10.1016/0010-2180(94)00147-K.
- [4] E. J. Highwood and R. P. Kinnersley, "When smoke gets in our eyes: The multiple impacts of atmospheric black carbon on climate, air quality and health," *Environ. Int.*, vol. 32, no. 4, pp. 560–566, 2006, doi: 10.1016/j.envint.2005.12.003.
- [5] T. C. Bond and R. W. Bergstrom, "Light absorption by carbonaceous particles: An investigative review," *Aerosol Sci. Technol.*, vol. 40, no. 1, pp. 27–67, 2006, doi: 10.1080/02786820500421521.
- [6] M. E. Monge *et al.*, "Light changes the atmospheric reactivity of soot," *Proc. Natl. Acad. Sci. U. S. A.*, vol. 107, no. 15, pp. 6605–6609, 2010, doi: 10.1073/pnas.0908341107.
- [7] G. Mastrangelo, E. Fadda, and V. Marzia, "Polycyclic aromatic hydrocarbons and cancer in man.," *Environ. Health Perspect.*, vol. 104, no. 11, p. 1166, 1996.
- [8] O. Boucher *et al.*, "Clouds and Aerosols," in *Climate Change 2013: The Physical Science Basis. Contribution of Working Group I to the Fifth Assessment Report of the Intergovernmental Panel on Climate Change*, T. F. Stocker, D. Qin, G.-K. Plattner, M. Tignor, S. K. Allen, J. Boschung, A. Nauels, Y. Xia, V. Bex, and P. M. Midgley, Eds. Cambridge, United Kingdom and New York, NY, USA: Cambridge University Press, 2013, pp. 571–658.
- [9] G. Myhre *et al.*, "Anthropogenic and Natural Radiative Forcing," in *Climate Change 2013: The Physical Science Basis. Contribution of Working Group I to the Fifth Assessment Report of the Intergovernmental Panel on Climate Change*, T. F. Stocker, D. Qin, G.-K. Plattner, M. Tignor, S. K. Allen, J. Boschung, A. Nauels, Y. Xia, V. Bex, and P. M. Midgley, Eds. Cambridge, United Kingdom and New York, NY, USA: Cambridge University Press, 2013, pp. 659–740.
- [10] J. Dong, J. M. Zhao, and L. H. Liu, "Morphological effects on the radiative properties of soot aerosols in different internally mixing states with sulfate," *J. Quant. Spectrosc. Radiat. Transf.*, vol. 165, pp. 43–55, 2015, doi: 10.1016/j.jqsrt.2015.06.025.
- [11] D. Müller *et al.*, "Microphysical particle parameters from extinction and backscatter lidar data by inversion with regularization: experiment," *Appl. Opt.*, vol. 39, no. 12, p. 1879, 2000, doi: 10.1364/ao.39.001879.
- [12] A. Miffre, G. David, B. Thomas, and P. Rairoux, "Atmospheric non-spherical particles optical properties from UV-polarization lidar and scattering matrix," *Geophys. Res.*

- Lett.*, vol. 38, no. 16, 2011.
- [13] E. Chemyakin, S. Burton, A. Kolgotin, D. Müller, C. Hostetler, and R. Ferrare, "Retrieval of aerosol parameters from multiwavelength lidar: investigation of the underlying inverse mathematical problem," *Appl. Opt.*, vol. 55, no. 9, p. 2188, 2016, doi: 10.1364/ao.55.002188.
- [14] A. Miffre, D. Cholleton, and P. Rairoux, "On the use of light polarization to investigate the size, shape, and refractive index dependence of backscattering Ångström exponents," *Opt. Lett.*, vol. 45, no. 5, p. 1084, 2020, doi: 10.1364/ol.385107.
- [15] T. Mehri *et al.*, "Investigating the size, shape and surface roughness dependence of polarization lidars with light-scattering computations on real mineral dust particles: Application to dust particles' external mixtures and dust mass concentration retrievals," *Atmos. Res.*, vol. 203, no. October 2017, pp. 44–61, 2018, doi: 10.1016/j.atmosres.2017.11.027.
- [16] A. Miffre, D. Cholleton, T. Mehri, and P. Rairoux, "Remote sensing observation of new particle formation events with a (UV, VIS) polarization lidar," *Remote Sens.*, vol. 11, no. 15, 2019, doi: 10.3390/rs11151761.
- [17] G. David, B. Thomas, T. Nousiainen, A. Miffre, and P. Rairoux, "Retrieving simulated volcanic, desert dust and sea-salt particle properties from two/three-component particle mixtures using UV-VIS polarization lidar and T matrix," *Atmos. Chem. Phys.*, vol. 13, no. 14, pp. 6757–6776, 2013, doi: 10.5194/acp-13-6757-2013.
- [18] A. Miffre, C. Anselmo, S. Geffroy, E. Fréjafon, and P. Rairoux, "Lidar remote sensing of laser-induced incandescence on light absorbing particles in the atmosphere," *Opt. Express*, vol. 23, no. 3, p. 2347, 2015, doi: 10.1364/oe.23.002347.
- [19] M. Tesche *et al.*, "Vertically resolved separation of dust and smoke over Cape Verde using multiwavelength Raman and polarization lidars during Saharan Mineral Dust Experiment 2008," *J. Geophys. Res. Atmos.*, vol. 114, no. 13, pp. 1–14, 2009, doi: 10.1029/2009JD011862.
- [20] M. Kahnert and F. Kanngießer, "Modelling optical properties of atmospheric black carbon aerosols," *J. Quant. Spectrosc. Radiat. Transf.*, vol. 244, p. 106849, 2020, doi: 10.1016/j.jqsrt.2020.106849.
- [21] L. Liu and M. I. Mishchenko, "Scattering and radiative properties of morphologically complex carbonaceous aerosols: A systematic modeling study," *Remote Sens.*, vol. 10, no. 10, 2018, doi: 10.3390/rs10101634.
- [22] L. Liu and M. I. Mishchenko, "Spectrally dependent linear depolarization and lidar ratios for nonspherical smoke aerosols," *J. Quant. Spectrosc. Radiat. Transf.*, vol. 248, p. 106953, 2020, doi: 10.1016/j.jqsrt.2020.106953.
- [23] R. Ceolato, F. Gaudfrin, O. Pujol, N. Riviere, M. J. Berg, and C. M. Sorensen, "Lidar cross-sections of soot fractal aggregates: Assessment of equivalent-sphere models," *J. Quant. Spectrosc. Radiat. Transf.*, vol. 212, pp. 39–44, 2018, doi: 10.1016/j.jqsrt.2017.12.004.
- [24] H. Li, C. Liu, L. Bi, P. Yang, and G. W. Kattawar, "Numerical accuracy of 'equivalent' spherical approximations for computing ensemble-averaged scattering properties of fractal soot aggregates," *J. Quant. Spectrosc. Radiat. Transf.*, vol. 111, no. 14, pp. 2127–2132, 2010, doi: 10.1016/j.jqsrt.2010.05.009.
- [25] C. M. Sorensen, *Light scattering by fractal aggregates: A review*, vol. 35, no. 2. 2001.
- [26] Y. Zhao and L. Ma, "Applicable range of the Rayleigh-Debye-Gans theory for calculating the scattering matrix of soot aggregates," *Appl. Opt.*, vol. 48, no. 3, pp. 591–597, 2009, doi: 10.1364/AO.48.000591.
- [27] F. Liu, J. Yon, and A. Bescond, "On the radiative properties of soot aggregates - Part 2: Effects of coating," *J. Quant. Spectrosc. Radiat. Transf.*, vol. 172, pp. 134–145, 2016, doi: 10.1016/j.jqsrt.2015.08.005.
- [28] K. Adachi, S. H. Chung, and P. R. Buseck, "Shapes of soot aerosol particles and implications for their effects on climate," *J. Geophys. Res. Atmos.*, vol. 115, no. 15, pp. 1–9, 2010, doi: 10.1029/2009JD012868.
- [29] M. I. Mishchenko, L. Liu, and D. W. Mackowski, "T-matrix modeling of linear

- depolarization by morphologically complex soot and soot-containing aerosols," *J. Quant. Spectrosc. Radiat. Transf.*, vol. 123, pp. 135–144, 2013.
- [30] O. Muñoz *et al.*, "Experimental determination of scattering matrices of dust particles at visible wavelengths: The IAA light scattering apparatus," *J. Quant. Spectrosc. Radiat. Transf.*, vol. 111, no. 1, pp. 187–196, 2010, doi: 10.1016/j.jqsrt.2009.06.011.
- [31] M. Schnaiter, S. Büttner, O. Möhler, J. Skrotzki, M. Vragel, and R. Wagner, "Influence of particle size and shape on the backscattering linear depolarisation ratio of small ice crystals-cloud chamber measurements in the context of contrail and cirrus microphysics," *Atmos. Chem. Phys.*, vol. 12, no. 21, pp. 10465–10484, 2012, doi: 10.5194/acp-12-10465-2012.
- [32] A. Miffre, D. Cholleton, and P. Rairoux, "Laboratory evaluation of the scattering matrix elements of mineral dust particles from 176.0° up to 180.0°-exact backscattering angle," *J. Quant. Spectrosc. Radiat. Transf.*, vol. 222–223, pp. 45–59, 2019, doi: 10.1016/j.jqsrt.2018.10.019.
- [33] A. Miffre, T. Mehri, M. Francis, and P. Rairoux, "UV-VIS depolarization from Arizona Test Dust particles at exact backscattering angle," *J. Quant. Spectrosc. Radiat. Transf.*, vol. 169, pp. 79–90, 2016, doi: 10.1016/j.jqsrt.2015.09.016.
- [34] A. Gialitaki *et al.*, "Is the near-spherical shape the " new black " for smoke ? To cite this version : HAL Id : hal-02776682 Is the near – spherical shape the ' new black ' for smoke ?," pp. 0–29, 2020.
- [35] J. Liu, Q. Zhang, J. Wang, and Y. Zhang, "Light scattering matrix for soot aerosol: Comparisons between experimental measurements and numerical simulations," *J. Quant. Spectrosc. Radiat. Transf.*, vol. 246, p. 106946, 2020, doi: 10.1016/j.jqsrt.2020.106946.
- [36] S. P. Burton *et al.*, "Information content and sensitivity of the 3β + 2α lidar measurement system for aerosol microphysical retrievals," *Atmos. Meas. Tech.*, vol. 9, no. 11, pp. 5555–5574, 2016, doi: 10.5194/amt-9-5555-2016.
- [37] M. I. Mishchenko and M. A. Yurkin, "On the concept of random orientation in far-field electromagnetic scattering by nonspherical particles," *Opt. Lett.*, vol. 42, no. 3, p. 494, 2017, doi: 10.1364/ol.42.000494.
- [38] M. I. Mishchenko, *Electromagnetic scattering by particles and particle groups: an introduction*. Cambridge University Press, 2014.
- [39] M. I. Mishchenko, L. D. Travis, and A. a Lacis, "Scattering, Absorption, and Emission of Light by Small Particles," *Vasa*, pp. 1–486, 2002.
- [40] G. Parent *et al.*, "Spectral radiation emitted by kerosene pool fires," *Fire Saf. J.*, vol. 108, no. January, p. 102847, 2019, doi: 10.1016/j.firesaf.2019.102847.
- [41] S. P. Kearney and F. Pierce, "Evidence of soot superaggregates in a turbulent pool fire," *Combust. Flame*, vol. 159, no. 10, pp. 3191–3198, 2012, doi: 10.1016/j.combustflame.2012.04.011.
- [42] G. Heskestad, "Fire plumes, flame height, and air entrainment," in *SFPE handbook of fire protection engineering*, Springer, 2016, pp. 396–428.
- [43] P. H. Thomas, "The size of flames from natural fires. In 'Ninth Symposium (International) on Combustion', 27 August–1 September 1962, Pittsburgh, PA." Academic Press: New York, 1963.
- [44] T. L. Farias, Ü. Ö. Köylü, and M. G. Carvalho, "Effects of polydispersity of aggregates and primary particles on radiative properties of simulated soot," *J. Quant. Spectrosc. Radiat. Transf.*, vol. 55, no. 3, pp. 357–371, 1996, doi: 10.1016/0022-4073(95)00166-2.
- [45] D. Huang, C. Guo, and L. Shi, "Experimental investigation on the morphology of soot aggregates from the burning of typical solid and liquid fuels," *J. Nanoparticle Res.*, vol. 19, no. 3, 2017, doi: 10.1007/s11051-017-3786-x.
- [46] M. L. Eggersdorfer and S. E. Pratsinis, "The structure of agglomerates consisting of polydisperse particles," *Aerosol Sci. Technol.*, vol. 46, no. 3, pp. 347–353, 2012, doi: 10.1080/02786826.2011.631956.
- [47] D. W. Mackowski, "Electrostatics analysis of radiative absorption by sphere clusters in

- the Rayleigh limit: application to soot particles," *Appl. Opt.*, vol. 34, no. 18, p. 3535, 1995, doi: 10.1364/ao.34.003535.
- [48] D. W. Mackowski, "A simplified model to predict the effects of aggregation on the absorption properties of soot particles," *J. Quant. Spectrosc. Radiat. Transf.*, vol. 100, no. 1–3, pp. 237–249, 2006, doi: 10.1016/j.jqsrt.2005.11.041.
- [49] C. M. Sorensen, "The mobility of fractal aggregates: A review," *Aerosol Sci. Technol.*, vol. 45, no. 7, pp. 765–779, 2011, doi: 10.1080/02786826.2011.560909.
- [50] J. Morán, A. Fuentes, F. Liu, and J. Yon, "FracVAL: An improved tunable algorithm of cluster–cluster aggregation for generation of fractal structures formed by polydisperse primary particles," *Comput. Phys. Commun.*, vol. 239, pp. 225–237, 2019, doi: 10.1016/j.cpc.2019.01.015.
- [51] L. Paulien, R. Ceolato, L. Soucasse, F. Enguehard, and A. Soufiani, "Lidar-relevant radiative properties of soot fractal aggregate ensembles," *J. Quant. Spectrosc. Radiat. Transf.*, vol. 241, 2020, doi: 10.1016/j.jqsrt.2019.106706.
- [52] C. Liu, Y. Yin, F. Hu, H. Jin, and C. M. Sorensen, "The Effects of Monomer Size Distribution on the Radiative Properties of Black Carbon Aggregates," *Aerosol Sci. Technol.*, vol. 49, no. 10, pp. 928–940, 2015, doi: 10.1080/02786826.2015.1085953.
- [53] D. W. Mackowski, "MSTM A multiple sphere T-matrix FORTRAN code for use on parallel computer clusters," pp. 1–36, 2013.
- [54] A. Bescond, Jérôme Yon, T. Girasole, C. Jouen, C. Rozé, and A. Coppalle, "Numerical investigation of the possibility to determine the primary particle size of fractal aggregates by measuring light depolarization," *J. Quant. Spectrosc. Radiat. Transf.*, vol. 126, pp. 130–139, 2013, doi: 10.1016/j.jqsrt.2012.10.011.
- [55] J. Yon, F. Liu, J. Morán, and A. Fuentes, "Impact of the primary particle polydispersity on the radiative properties of soot aggregates," *Proc. Combust. Inst.*, vol. 37, no. 1, pp. 1151–1159, 2019, doi: 10.1016/j.proci.2018.07.065.
- [56] M. Schnaiter, H. Horvath, O. Möhler, K. H. Naumann, H. Saathoff, and O. W. Schöck, "UV-VIS-NIR spectral optical properties of soot and soot-containing aerosols," *J. Aerosol Sci.*, vol. 34, no. 10, pp. 1421–1444, 2003, doi: 10.1016/S0021-8502(03)00361-6.
- [57] M. Wentzel, H. Gorzawski, K. H. Naumann, H. Saathoff, and S. Weinbruch, "Transmission electron microscopical and aerosol dynamical characterization of soot aerosols," *J. Aerosol Sci.*, vol. 34, no. 10, pp. 1347–1370, 2003, doi: 10.1016/S0021-8502(03)00360-4.
- [58] Y. Wu, T. Cheng, L. Zheng, and H. Chen, "Effect of morphology on the optical properties of soot aggregated with spheroidal monomers," *J. Quant. Spectrosc. Radiat. Transf.*, vol. 168, pp. 158–169, 2016, doi: 10.1016/j.jqsrt.2015.09.017.
- [59] W. Kim, C. M. Sorensen, and A. Chakrabarti, "Universal occurrence of soot super-aggregates with a fractal dimension of 2.6 in heavily sooting laminar diffusion flames," *Langmuir*, vol. 20, no. 10, pp. 3969–3973, 2004, doi: 10.1021/la036085+.
- [60] C. M. Sorensen, W. Kim, D. Fry, D. Shi, and A. Chakrabarti, "Observation of soot superaggregates with a fractal dimension of 2.6 in laminar acetylene/air diffusion flames," *Langmuir*, vol. 19, no. 18, pp. 7560–7563, 2003, doi: 10.1021/la034063h.
- [61] R. Ceolato, L. Paulien, J. B. Maughan, C. M. Sorensen, and M. J. Berg, "Radiative properties of soot fractal superaggregates including backscattering and depolarization," *J. Quant. Spectrosc. Radiat. Transf.*, vol. 247, p. 106940, 2020, doi: 10.1016/j.jqsrt.2020.106940.
- [62] C. Weitkamp, *Lidar : range-resolved optical remote sensing of the atmosphere*, no. 102. 2005.